University of Bristol - Explore Bristol Research
General rights

Acoustic Hologram Enhanced Phased Arrays for Ultrasonic Particle Manipulation

Luke Cox[1,*] Kai Melde[2] Anthony Croxford,[1] Peer Fischer,[2,3] and Bruce W. Drinkwater[1]

[1]*Department of Mechanical Engineering, University of Bristol, Bristol BS8 1TR, United Kingdom*
[2]*Max Planck Institute for Intelligent Systems, Heisenbergstrasse 3, 70569 Stuttgart, Germany*
[3]*Institute of Physical Chemistry, University of Stuttgart, Pfaffenwaldring 55, 70569 Stuttgart, Germany*

The ability to shape ultrasound fields is important for particle manipulation, medical therapeutics, and imaging applications. If the amplitude and/or phase is spatially varied across the wave front, then it is possible to project "acoustic images." When attempting to form an arbitrary desired static sound field, acoustic holograms are superior to phased arrays due to their significantly higher phase fidelity. However, they lack the dynamic flexibility of phased arrays. Here, we demonstrate how to combine the high-fidelity advantages of acoustic holograms with the dynamic control of phased arrays in the ultrasonic frequency range. Holograms are used with a 64-element phased array, driven with continuous excitation. Movement of the position of the projected hologram via phase delays that steer the output beam is demonstrated experimentally. This allows the creation of a much more tightly focused point than with the phased array alone, while still being reconfigurable. It also allows the complex movement at a water-air interface of a "phase surfer" along a phase track or the manipulation of a more arbitrarily shaped particle via amplitude traps. Furthermore, a particle manipulation device with two emitters and a single split hologram is demonstrated that allows the positioning of a "phase surfer" along a one-dimensional axis. This paper opens the door for new applications with complex manipulation of ultrasound while minimizing the complexity and cost of the apparatus.

I. INTRODUCTION

Holography is the spatial storage of the phase and/or amplitude profile of a desired wave form [1,2]. A coherent beam is passed through the hologram and the interference generates the desired wave form. This effect is most well known in optics but has previously been demonstrated successfully in underwater ultrasound using three-dimensional (3D) printed holograms [3]. In ultrasound, the traditional technique for generating a desired sound field is to use a phased array consisting of a number of independently controlled elements [4–9]. However, the hologram offers two key advantages; the first is the simplification of the driving electronics, as it only requires a single channel [10], and the second is the increased phase fidelity, which is only limited by the print or machining resolution. The major weakness of the holographic technique with a single source is the inability to dynamically reconfigure the field. Some dynamic updating has been achieved by encoding multiple images into a single hologram, each sensitive to different frequencies [11]. However, this approach is limited by the frequencies available to the transducer

at a reasonable amplitude. Furthermore, having only distinct frequency separated fields limits the possibilities for the smooth continuous motion that is desirable in particle manipulation. The integration of a phased array with a phase-delay surface has been demonstrated in air with a focused self-bending beam [12]. We note that the operation in water presented here offers a significant simplification over this previous work, as there is no requirement for the complex labyrinth-type delay lines commonly employed when operating in air. We demonstrate the capabilities of combining the dynamic phased array with the static hologram applied to particle manipulation.

Particle manipulation is an area of growing interest for a variety of applications, particularly in the fields of pharmaceutics, biology, and chemistry [13–21], due to its ability to interact with any material and its proven ability not to damage the viability of cells [22–24]. It is also a suitable candidate for emerging applications such as the delivery of food [25] and the creation of dynamic 3D displays [26]. Acoustic holograms produced by 3D printing have been demonstrated as being capable of trapping [27] and assembling [28] particles; however, this has all been achieved with static fields and particle movement obtained via physical movement of a positioning stage, particle buoyancy, or

*luke.cox@bristol.ac.uk

static phase gradients. Here, in contrast to previous work [27,29,30], dynamic particle manipulation in a variety of forms is demonstrated by control of a complex acoustic field with no moving parts.

Section II numerically examines the differences in potential fidelity between a phased array and a hologram and their consequences. Section III demonstrates the capabilities and limitations of using a phased array in combination with a hologram. Section IV demonstrates a manipulation technique using only two emitting transducers combined with a split hologram to manipulate a particle along a one-dimensional (1D) axis.

II. INFORMATION DENSITY

One of the most significant practical advantages of an acoustic hologram over a phased array is the higher information density, which scales with the number of independent inputs to the system. For a phased array, this is equivalent to the number of individual transducer elements. For a printed acoustic hologram, this translates to the surface features that can be resolved by the reconstructing wave (i.e., pixels of diffraction-limited size).

A simulation study is conducted to investigate these effects on the creation of a desired sound field. Figure 1 illustrates the performance of a typical commercial phased array versus a 3D-printed hologram. Here, an 11×11 array (121 elements, pitch equals 4.55 mm) is used, which is typical of both medical imaging and nondestructive testing devices. We note that while arrays with around 1000 elements have been constructed [31], this is still an order of magnitude less than is readily obtainable in a 3D-printed hologram. The 3D-printed hologram has 134×134 pixels,

with a pitch of 0.37 mm, and is typical of that achieved by a medium-quality 3D printer. The letter "R" is chosen as a target shape for its variety of features and relative simplicity. An iterative angular-spectrum approach (IASA) [3] is used to calculate the phase distribution needed to generate the desired output acoustic field. The projection plane is 25 mm above a 50 mm $\times$ 50 mm-square hologram plane, with an excitation frequency of 2 MHz to reflect the available experimental equipment. The "R" shape is 42 mm $\times$ 19 mm wide and is positioned in the center of the projection plane. Initially, the phase distribution is calculated using the IASA at a very high resolution of 334×334 pixels with a pitch of 0.15 mm. This defines the input phases necessary at the hologram plane. This solution is down-sampled by averaging across larger overlaid grid squares to represent the printer resolution limit for the 3D-printed holographic surfaces or the array element size for the phased array. This output is then propagated forward into the projection plane using the angular-spectrum approach, as detailed in Ref. [3]. To compare the performances, the correlation of the pressure amplitudes of the obtained acoustic field and the target are calculated for each case.

An investigation is also conducted by directly simulating the hologram at the 134×134 resolution and the difference in outcomes between this and the down-sampling approach is found to be negligible, suggesting that both approaches are valid.

The same down-sampling technique is applied at a wider range of array sizes to generate Fig. 2. This shows the increase in the correlation coefficient of the image as the number of elements or pixels increases and highlights the superiority of the hologram in this regard. However, despite the improved image quality obtainable with the hologram when compared to the array, the hologram creates a static field, whereas the array is capable of real-time reconfiguration, e.g., enabling the beam to be steered over
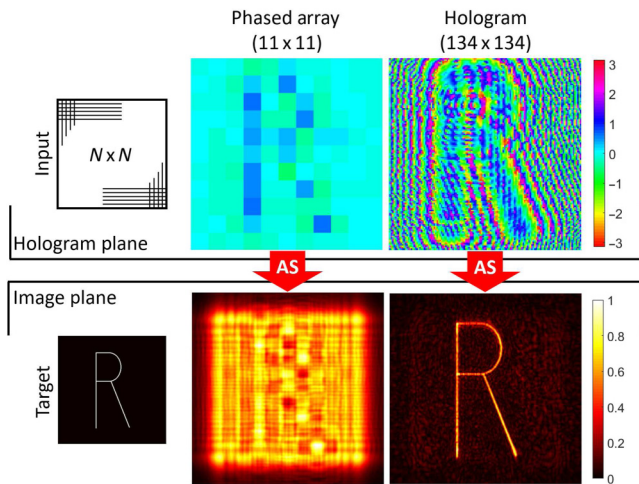

FIG. 1.   A comparison of the possible phase inputs and sound-pressure-amplitude outputs for typical element or pixel numbers of phased arrays and 3D-printed holograms, respectively. The fields are propagated using the angular-spectrum method (labelled as AS).
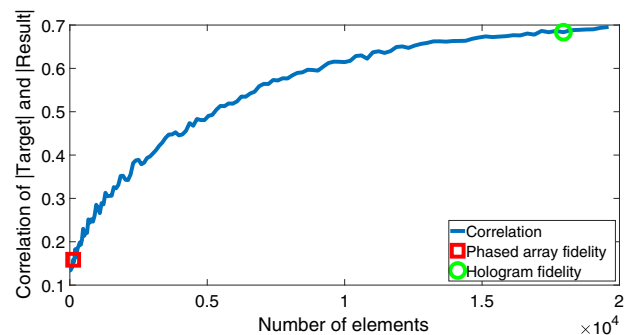

FIG. 2.   A graph showing the correlation between the target and output amplitude for an "R" shape from a simulated phase-delay plane. The markers represent the images in Fig. 1; the phased-array resolution is 11×11 elements, i.e., 121 channels, while the hologram has 134×134 pixels, i.e., 17 956 pixels in total.

a range of angles or focused at a range of points. This paper now explores the possibilities that emerge when these two devices are combined.

III. BEAM-STEERED PHASED ARRAYS

In this section, a phased array is used to reconfigure the output of a hologram. A selection of 3D-printed holograms is used in combination with an Imasonic 6363A101 2 MHz, 64-element 1D linear transducer array with an element pitch of 1.57 mm and a width of 22 mm. The holograms are 3D printed (Object Connex 260, Stratasys) using a VeroClear polymer compound (Stratasys) at a print cost in the order of U.S.$20 circa September 2019. This hologram is shaped to fit on top of the 22 mm × 100 mm array. In the 3D-printed holograms, each 0.37 mm × 0.37 mm pixel has a material thickness determined by the required phase delay.

The signals for the phased array are generated by a field-programmable-gate-array (FPGA) chip on a breakout board (CoreEP4CE10, Waveshare). This generates square waves and a full 2π of phase is discretized into 64 parts, meaning that the phase resolution is 0.098 rad. The individual phases are controlled from a computer via MATLAB. The signals are amplified using a custom driver board with MOSFET amplifiers for each channel.

As shown in Fig. 3, the experiment is set up with the projection plane at the water's surface. The hologram is placed in contact with the surface of the array and coupled to the array with Coupling Gel (W250, Sonatest Ltd.). Further experimental details can be found in the Supplemental Material [32].

A. Steering a phased-array plane wave

If all transducers are operated in phase, the field produced directly in front of the array will be a reasonable approximation of a plane wave due to the large size of the emitting surface [33]. By applying a phase gradient across
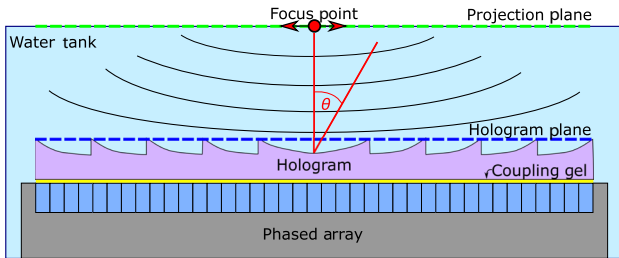

FIG. 3. A diagram of the phased array and hologram system used in the experiments. A 64 element array at the bottom is able to steer the plane-wave output. This array is coupled to the 3D-printed hologram with a coupling gel. The red dot represents a particle trapped in the projection plane and moved in the directions indicated.

the array, this output plane wave can be steered, to propagate at a different angle. The phase delay applied to each transducer is given by

$$\Delta\phi = \frac{2\pi d \sin(\theta_s)}{\lambda}, \quad (1)$$

where $\Delta\phi$ is the change in the input phase between each neighboring array element (in radians), d is the pitch between element centers of the array, θ_s is the steering angle desired (in radians), and λ is the ultrasonic wavelength [34].

The wave propagation through the medium is simulated using the angular-spectrum method. Initially, the hologram is calculated to form a focus at $0°$ (i.e., normal to the array surface) in the projection plane, as shown in Fig. 3. Another simulation plane, $A(\theta_s)$, coincident with the hologram plane, H, is then created to represent the array and the steering. The output magnitude is set equal to 1 where the transducer elements are present (and 0 in the gaps between them). To achieve dynamic manipulation, each element is then adjusted to have the emitted phase ϕ_s necessary to produce the steering angle θ_s, as calculated in Eq. (1). The magnitude is assumed to remain constant while propagating through the hologram so that the final net propagation plane, called P (at the same location as H), is then calculated by

$$P = |A(\theta_s)|e^{i[\angle H + \angle A(\theta_s)]}. \quad (2)$$

P is then propagated through the water to the specified projection plane (shown in orange in Fig. 3) using the angular-spectrum method to produce the predicted steered output. Further details and diagrams can be found in the Supplemental Material [32].

B. Visualization with a thermochromic sheet

To visualize the sound fields and validate the simulations, a liquid-crystal thermochromic color-changing sheet (150 mm × 150 mm, 0.31 mm thickness, 20 °C–25 °C sensitivity, SFXC) is fixed onto a frame that holds it at the hologram imaging plane at the surface of the water, 25 mm above the phased array. The color of the thermochromic film changes in response to acoustic pressure induced temperature changes [35]. A comparison between the simulated acoustic pressure and experimental results from the thermochromic film is shown in Fig. 4.

The voltage required to drive each transducer is such that, when they are all driven in phase, the power supply cannot give enough power to excite them all with sufficient output amplitude for manipulation or visualization with the thermochromic sheet. Hence, a minimum steering angle of $0.25°$ is used.

The first comparison made is between focusing the array without a hologram and a focused point with a hologram.
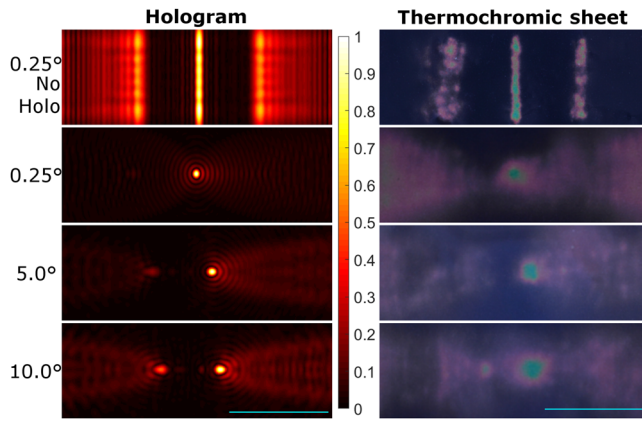
FIG. 4. A selection of comparisons between the simulated results (acoustic pressure) and photographs of the thermochromic sheet (indicating the temperature rise) in the same conditions. In the top image, "No Holo" indicates a comparison without a hologram on the phased array. In all others, the same focused-point hologram is attached. The phase maps applied to the arrays are shown in the Supplemental Material [32]. All simulated results are normalized. The scale bars represent 20 mm.

From Fig. 4, it can be seen that with no hologram there are significant grating lobes in the image plane. Furthermore, there is no focusing effect out of the axis of the array, generating the wide focus line. This is in direct contrast to the hologram, where both theoretically and experimentally the resulting pressure distribution is a tightly focused point. The reduction in the grating lobes is also significant: without the hologram, the grating lobes are at −4.89 dB, while with the hologram, the grating lobes are −23.21 dB relative to the main lobe.

Figure 4 shows generally good agreement between the simulation and the experiment. There is some deviation in the size of the focal region seen in the experimental thermochromic sheets, as opposed to the small simulated focal regions. This is believed to be due to the conduction of heat away from the maximum-temperature point, indicating a weakness in the indirect measurement of the pressure through temperature.

Note that as the steering angle increases, a significant grating artifact begins to appear. It can be seen that at a $10°$ steering angle, the grating artifact is already approaching the magnitude of the desired focus. This aliasing is a result of the array used having element pitch, d, larger than $\lambda/2$ ($\lambda = 0.75$ mm and $d = 1.57$ mm). Similar effects will occur with more complex shapes, e.g., at high steering angles, two copies of the image will appear side by side. This is shown in more detail in the Supplemental Material [32]. However, this is not a fundamental problem; the artifact can be completely removed with an array element pitch less than half the wavelength.

C. Focused-point manipulation

A single focused point at the water-air interface can be used to manipulate a suitable particle via surface deformation and tension. By positioning a polymer-foam circular-disk- (Aptflex F48, Precision Acoustics Ltd., U.K.) shaped particle of 4.0 mm diameter onto the peak generated on the surface of the water by the high acoustic pressure field, it will remain in place due to the balance of surface-tension forces [3]. By moving this focal spot smoothly along the air-water interface, the particle will move with it, allowing precise manipulation.

Figure 5(a) shows that this surface-focal-point movement technique is able to move the 4.0-mm-diameter disk over a distance of 14.4 mm. Figure 5(b) shows the locations (traced by Tracker 4.93, Open Source Physics) from a video (Nikon D610 camera) compared to that theoretically predicted by the angular-spectrum method, with good agreement. A small systematic error is seen in both directions, which is thought to be due to a slight misalignment between the hologram and the array. The average of the absolute difference between the predicted and experimental location in the x direction of motion is 1.00 mm, while in the y direction it is 0.01 mm.

Attempts are made to transport the same particle using focusing without the hologram (see the first row of Fig. 4
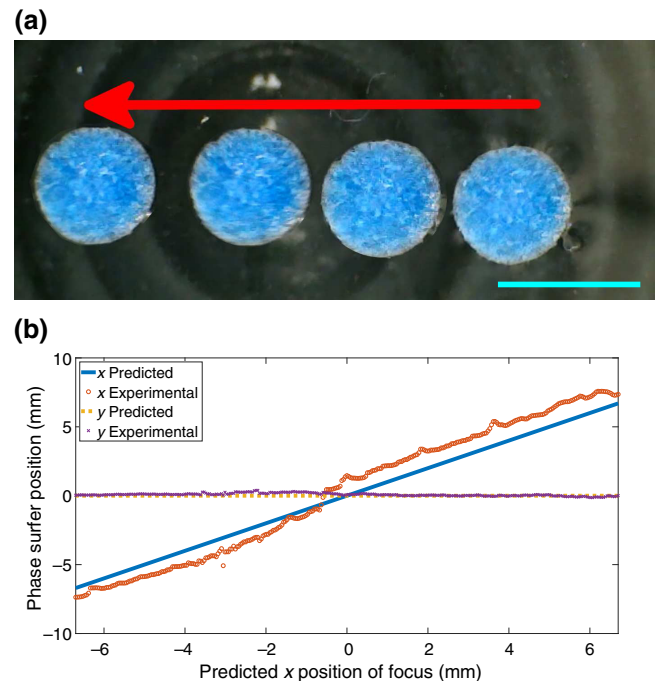
(a)

(b)

FIG. 5. The movement of the phase surfer with the focus point over a range of $−15°$ to $+15°$. (a) A compound photograph of the phase surfer moving with the focus point. (b) A graph of the expected focus location and traced location of the phase surfer. The scale bar is 5 mm. See Supplemental Video 1 in the Supplemental Material [32].

for the pressure field without the hologram) but these are unsuccessful. The particle quickly drifts away from the focused line, often before the line starts moving. This demonstrates the superiority of the hologram focusing technique for these purposes. The tracking also validates our understanding of the operating principle of the manipulation.

However, similar focusing is achievable via other techniques, e.g., using multirowed phased arrays. Therefore, the next section presents an example of the manipulation of a phase surfer, which cannot be achieved by an array alone without a significantly larger number of array elements, truly exploiting the capability of the combined method.

D. Phase-circle manipulation

More complex manipulation is presented in this section. The 4.0-mm-diameter disk, as described in Sec. III C, will follow a phase-ramp track along the surface of the water, in a technique termed phase surfing [3].

A circle of high pressure is projected at the water-air interface, as shown in Fig. 6(a). This generates a circular ridge, on the peak of which a disk is trapped by surface tension, as it was in the previous section at the focus point. This ridge also has a phase gradient present, as shown in Fig. 6(b). This gradient propels the disk around the ridge upon which it is trapped. Here, a circular phase-ramp track, of radius 3 mm, with a total phase change of 4π around the circumference is created at a distance of 25 mm. In our case, the motion of the disk is in an anticlockwise direction. The array steering is then applied and this circular track can be moved, along with the particle. The two types of independent motion are illustrated in Fig. 7(a).

The tracking of the particle motion is shown in Fig. 7(b). It can be seen that the particle follows the desired circular path with reasonable accuracy. The maximum divergence from the predicted circular path occurs at $3°$ of steering, which is the maximum attempted (for further

(a)

(b)

FIG. 7. The behavior of the phase surfer on the circular phase gradient path. (a) A schematic representation of the motion of the phase surfer on the circular phase-gradient track. The green arrow indicates the circular movement induced by the phase-gradient track, while the red arrow indicates the linear movement of this entire track due to the steering of the phased array. The scale bar is 5 mm. (b) The tracked paths of the phase surfer as the beam is steered from an angle of $3°$ to $-3°$. The paths of different colors represent different steering angles. The correspondingly colored crosses are the experimental path centers and the circles the theoretical path centers. For video, see Supplemental Video 2 in the Supplemental Material [32].
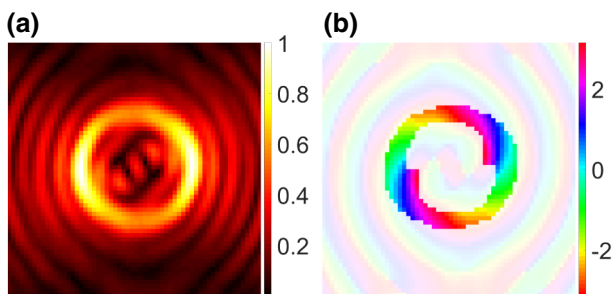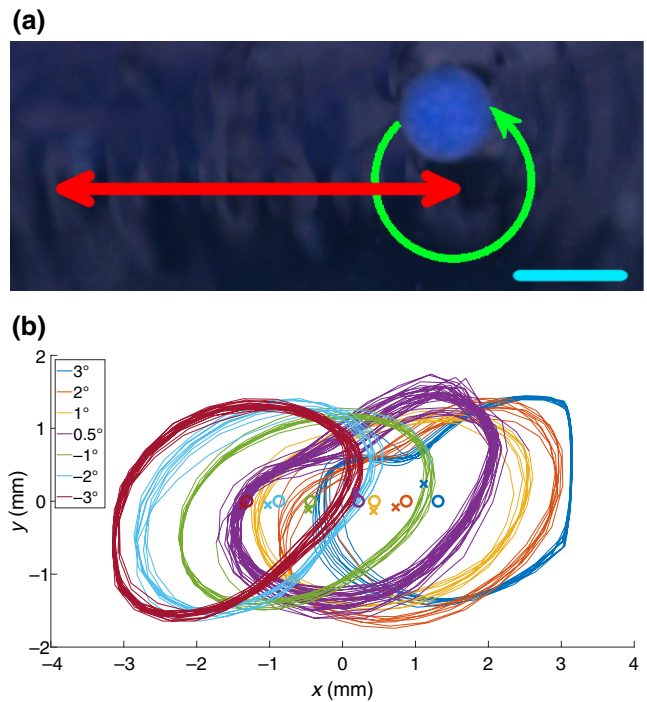
FIG. 6. The projected (a) amplitude and (b) phases of the phase-gradient circle at a projection plane 25 mm above the hologram plane and at a steering angle of $0°$. The radius of the circle is 3 mm and the total phase change around the circle is 4π. The hologram plane used to produce this is shown in the Supplemental Material [32].

details of the errors, see the Supplemental Material [32]). These observed differences between the desired and actual positions are thought to be due to a combination of (i) amplitude variation around the circle, (ii) departure from a uniform phase ramp round the circle, and (iii) a "blurring" of the phase in the radial direction. These three features have all been observed in the angular-spectrum simulation of the array-hologram combination and are thought to stem from the use of a rectangular array and hologram (i.e., 100 mm × 22 mm in the holographic plane) to create a circular pressure field (i.e., the 3-mm-diameter circle). This inevitably means that more energy is directed toward some regions of the circle than others. An axis-symmetric array and/or the addition of amplitude control may allow improved reconstruction.

The average speed of the particle around the track is 23 mm/s, which corresponds to an average angular velocity of 1.22 rad/s. However, the speed changes as it rotated around the circle, with a lower velocity in the x direction (parallel to the largest array dimension) and a higher velocity when

travelling in the y direction. This is thought to be due to the uneven forces caused by the asymmetrical excitation discussed above. The fastest average speed is observed at the smallest steering angle ($0.5°$), which is also closest in shape and center location to that desired and therefore could be expected to have the most consistent forces on the phase surfer.

There is an additional application of circles (and potentially other closed forms) in the surface-based manipulation of larger and arbitrarily shaped particles. The dip in amplitude in the center of the circle [as shown in Fig. 6(a)] results in a local trough. Particles introduced into this surface trough remain trapped by gravity and can then be manipulated by translation of the trough location. Figure 8(a) shows the manipulation of an expanded polystyrene sphere (diameter 4.4 mm) in the x direction of 12.2 mm, equivalent to $-13°$ to $+13°$. As this surface-profile-based manipulation is not dependent on the phase profile around the circular ridge, it is possible to successfully translate particles over a much larger range than when using the same profile for a phase-gradient track. From Fig. 8(b), it can be seen that the manipulation position is in good agreement with the theory; the average of the absolute difference is 0.20 mm in the x-axis direction of motion and 0.14 mm in the y-axis direction. This positioning is found to be more precise than the focal-point
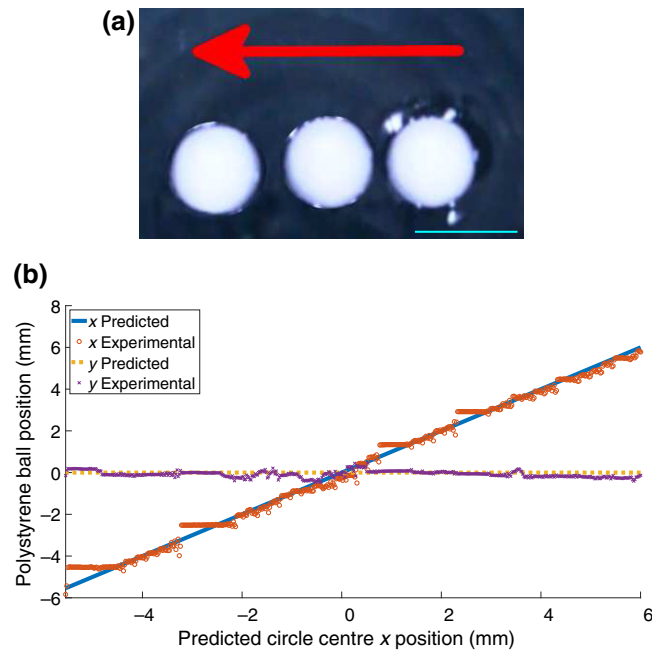

FIG. 8. The behavior of a 4.4-mm-diameter expanded-polystyrene ball in the 3-mm-radius high-pressure circle being tilted from $13°$ to $-13°$. (a) A compound photograph of the sphere's movement from right to left, with a 5-mm scale bar. (b) The position tracking of the sphere in the x and y directions. For video, see Supplementary Video 3 in the Supplemental Material [32].

manipulation and we note that the trapping in this case is due to a local minimum in gravity, as opposed to a local minimum in capillary energy as in Sec. III C [3]. This technique can be applied to a wide range of particles, as any particle that fits within the trough is trapped. This could allow the design of a hologram for movement of a specific shape of object without rotation (e.g., a cube could be held with a square-shaped ridge) and without the need for switching electronics [36] or the significant complex computation [37] that previous techniques have involved. Furthermore, while the acoustic field required is more complex in form relative to focal trapping, there is no additional challenge in manufacturing the hologram and no increase in the electrical complexity.

IV. TWO ELEMENT MANIPULATION

This section details a phase-ramp-interaction-manipulation (PRIM) method and we demonstrate the manipulation of a particle along a 1D axis using just two transducer channels combined with a split hologram.

As shown in Fig. 9, a split hologram is placed above a single circular piezoelectric element with the electrical contacts split into two parts to separate the fields produced [27]. The split hologram is a single piece with two independently designed halves, with the hologram dividing line above the dividing line of the electrical contacts. Each half of the hologram creates a phase-ramp line in the x direction, similar in concept to the circular phase ramp described in the previous section. The line from one half drives the surfer in the positive x direction and the line for the other half drives in the negative x direction. When both sides are excited with matching amplitudes, they create opposing phase ramps that cancel each other out. By adjusting the relative voltages applied to the transducers, either one direction or the other can be made dominant,
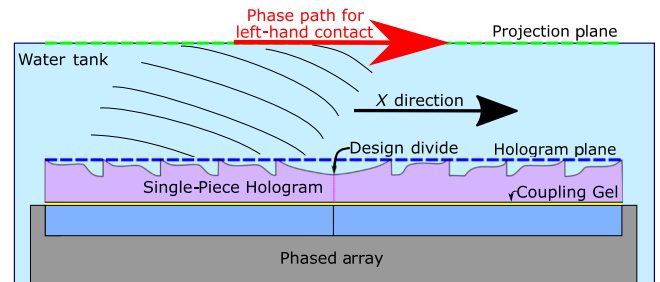

FIG. 9. A diagram of the setup for the two-element PRIM technique. The phased array in this case is made from a single piece of piezoelectric material, with the contacts split into two halves. The hologram is a single piece placed over these; however, it is designed in two independent halves. Both halves generate phase paths in opposite directions. In this case, the path is shown for the left-hand element, to create motion in the positive x direction. The right-hand element will produce a path in the negative x direction.
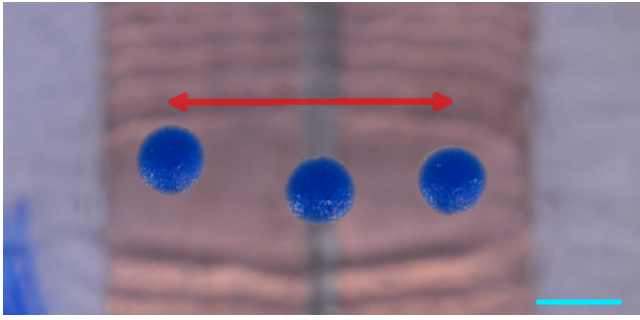
FIG. 10. A compound photograph of the phase surfer on the two-transducer PRIM setup. It can be held at any position along the line by adjusting the relative magnitudes of the transducer outputs. The scale bar is 5 mm. For video, see Supplementary Video 4 in the Supplemental Material [32].

propelling the particle in the desired direction along the linear track. Some positions in which the particle is held are shown in Fig. 10.

Each transducer produces a phase ramp of 20 mm in length with a total phase difference of 4π. The center of the line is above the center of the split contacts, as shown in Fig. 9. The projection plane is 15 mm above the hologram plane on the water-air interface. The phase map of the hologram used is shown in the Supplemental Material [32]. The piezo disk (PIC151 material piezo, PI Ceramic GmbH) has a nominal frequency of 1.94 MHz and fine tuning is used to match the exact resonant frequency of each of the separated sides. The electrical contacts from each transducer are then connected to separate arbitrary wave-form generators (Agilent 33220A) and amplifiers (AR75A250A, ARUK), to provide two channels of independent control.

It is possible to achieve a desired position in the controlled x direction and maintain it (see Fig. 10). Furthermore, the range of potential locations is slightly larger than that produced by the focused-surface-point approach (17.6 mm vs 14.4 mm). We note that this PRIM technique could be extended to a wide range of trajectories. The manipulation with this technique is not as accurate as that achieved in the previous sections. The tuning of relative amplitudes does not allow the specification of an exact location. Additionally, there is more visible deviation from the desired direction of motion, i.e., the desired motion is in the x direction and the particle is also seen to move in the y direction. This y-direction movement is thought to be due to the lower acoustic pressure generated by the two transducers relative to the array described in the previous sections, which leads to lower surface-tension forces relative to previous experiments. The mean absolute deviation in the y direction from the expected zero line is 0.32 mm, higher than any of the previous arrangements. The full tracked path can be seen in the Supplemental Material [32].

V. SUMMARY AND CONCLUSIONS

We show that combining a multielement phased array with a static hologram enables the generation of more complex dynamic ultrasound fields, which is promising for applications including particle manipulation.

A numerical study of the relative performances of phased arrays and holograms, based on their potential spatial phase discretization, is presented for the generation of a complex sound field. This highlights the superiority of holograms in terms of generating a complex field at low cost.

The combination of holograms with phased arrays is explored in both simulations and experiments. In particular, two different particle manipulation approaches are proposed and experimentally validated. Each approach offers control of particles with no moving parts, which is favorable from a reliability and cost perspective.

We show that the steering of the output plane waves of a phased array can be used to move the location of an holographically projected acoustic field. The movement of this field is found to be limited by the steering abilities of the array rather than the hologram. A focused point is used to demonstrate the ability of the combined array-hologram, with excellent agreement between predicted and experimental manipulation of a small particle on the surface of a water tank. More complex motion is demonstrated using a phase surfer driven around a circular phase ramp. Furthermore, the same hologram is used to trap a larger particle in the trough formed on the surface of the water. The array is then used to translate this trap and the particle in a line, with high accuracy.

Finally, the PRIM approach is demonstrated, in which a phase surfer is positioned along a 1D axis using two emitting elements. Here, we use a split hologram to create two opposed phase ramps and the two emitters to activate them. In this way, only two electrical channels are needed and the control is achieved by the relative amplitudes. The results from this array-hologram combination open the door for further possible applications, particularly in the world of microassembly, where one can imagine its use in the construction of microscale conveyor belts, passing particles from one location to the next (with the paths aligned in the same direction) while allowing each transducer to be switched on for a short time, meaning that the particles can be stopped and started easily at various intervals.

This work enables further applications of acoustic manipulation by releasing phased arrays from their resolution limitations and holograms from their static ones.

All data required to reproduce these results are stored on Zenodo [38].

---

[1] D. Gabor, A new microscopic principle, Nature **161**, 777 (1948).

[2] E. N. Leith and J. Upatnieks, Reconstructed wavefronts and communication theory, JOSA **52**, 1123 (1962).

[3] K. Melde, A. G. Mark, T. Qiu, and P. Fischer, Holograms for acoustics, Nature **537**, 518 (2016).

[4] T. Fushimi, T. Hill, A. Marzo, and B. Drinkwater, Nonlinear trapping stiffness of mid-air single-axis acoustic levitators, Appl. Phys. Lett. **113**, 034102 (2018).

[5] A. Marzo and B. W. Drinkwater, Holographic acoustic tweezers, Proc. Natl. Acad. Sci. **116**, 84 (2019).

[6] A. Marzo, S. A. Seah, B. W. Drinkwater, D. R. Sahoo, B. Long, and S. Subramanian, Holographic acoustic elements for manipulation of levitated objects, Nat. Commun. **6**, 8661 (2015).

[7] A. Marzo, T. Corkett, and B. W. Drinkwater, Ultraino: An open phased-array system for narrowband airborne ultrasound transmission, IEEE Trans. Ultrason. Ferroelectr. Freq. Control **65**, 102 (2017).

[8] M. Prisbrey and B. Raeymaekers, Ultrasound Noncontact Particle Manipulation of Three-Dimensional Dynamic User-Specified Patterns of Particles in Air, Phys. Rev. Appl. **10**, 034066 (2018).

[9] M. Prisbrey, J. Greenhall, F. Guevara Vasquez, and B. Raeymaekers, Ultrasound directed self-assembly of three-dimensional user-specified patterns of particles in a fluid medium, J. Appl. Phys. **121**, 014302 (2017).

[10] A. Marzo, A. Ghobrial, L. Cox, M. Caleap, A. Croxford, and B. Drinkwater, Realization of compact tractor beams using acoustic delay-lines, Appl. Phys. Lett. **110**, 014102 (2017).

[11] M. D. Brown, B. T. Cox, and B. E. Treeby, Design of multi-frequency acoustic kinoforms, Appl. Phys. Lett. **111**, 244101 (2017).

[12] M. A. Norasikin, D. Martinez Plasencia, S. Polychronopoulos, G. Memoli, Y. Tokuda, and S. Subramanian, *The 31st Annual ACM Symposium on User Interface Software and Technology* (ACM, Berlin, Germany, 2018), p. 247.

[13] C. J. Benmore and J. K. R. Weber, Amorphization of Molecular Liquids of Pharmaceutical Drugs by Acoustic Levitation, Phys. Rev. X **1**, 011004 (2011).

[14] E. Brandt, Acoustic physics: Suspended by sound, Nature **413**, 474 (2001).

[15] D. J. Collins, T. Alan, K. Helmerson, and A. Neild, Surface acoustic waves for on-demand production of picoliter droplets and particle encapsulation, Lab Chip **13**, 3225 (2013).

[16] J. Greenhall, F. Guevara Vasquez, and B. Raeymaekers, Ultrasound directed self-assembly of user-specified patterns of nanoparticles dispersed in a fluid medium, Appl. Phys. Lett. **108**, 103103 (2016).

[17] F. Guo, Z. Mao, Y. Chen, Z. Xie, J. P. Lata, P. Li, L. Ren, J. Liu, J. Yang, M. Dao, *et al.*, Three-dimensional manipulation of single cells using surface acoustic waves, Proc. Natl. Acad. Sci. **113**, 1522 (2016).

[18] P. Li and T. J. Huang, Applications of acoustofluidics in bioanalytical chemistry, Anal. Chem. **91**, 757 (2018).

[19] A. Ozcelik, J. Rufo, F. Guo, Y. Gu, P. Li, J. Lata, and T. J. Huang, Acoustic tweezers for the life sciences, Nat. Methods **15**, 1021 (2018).

[20] M. Sesen, T. Alan, and A. Neild, Microfluidic on-demand droplet merging using surface acoustic waves, Lab Chip **14**, 3325 (2014).

[21] Z. Yang, K. L. Cole, Y. Qiu, I. M. Somorjai, P. Wijesinghe, J. Nylk, S. Cochran, G. C. Spalding, D. A. Lyons, and K. Dholakia, Light sheet microscopy with acoustic sample confinement, Nat. Commun. **10**, 669 (2019).

[22] S. Li, P. Glynne-Jones, O. G. Andriotis, K. Y. Ching, U. S. Jonnalagadda, R. O. Oreffo, M. Hill, and R. S. Tare, Application of an acoustofluidic perfusion bioreactor for cartilage tissue engineering, Lab Chip **14**, 4475 (2014).

[23] M. Ohlin, I. Iranmanesh, A. E. Christakou, and M. Wiklund, Temperature-controlled MPa-pressure ultrasonic cell manipulation in a microfluidic chip, Lab Chip **15**, 3341 (2015).

[24] B. Vanherberghen, O. Manneberg, A. Christakou, T. Frisk, M. Ohlin, H. M. Hertz, B. Önfelt, and M. Wiklund, Ultrasound-controlled cell aggregation in a multi-well chip, Lab Chip **10**, 2727 (2010).

[25] C. T. Vi, A. Marzo, D. Ablart, G. Memoli, S. Subramanian, B. Drinkwater, and M. Obrist, *Proceedings of the 2017 ACM International Conference on Interactive Surfaces and Spaces* (ACM, Brighton, United Kingdom, 2017), p. 161.

[26] T. Fushimi, A. Marzo, B. W. Drinkwater, and T. L. Hill, Acoustophoretic volumetric displays using a fast-moving levitated particle, Appl. Phys. Lett. **115**, 064101 (2019).

[27] A. Franklin, A. Marzo, R. Malkin, and B. Drinkwater, Three-dimensional ultrasonic trapping of micro-particles in water with a simple and compact two-element transducer, Appl. Phys. Lett. **111**, 094101 (2017).

[28] K. Melde, E. Choi, Z. Wu, S. Palagi, T. Qiu, and P. Fischer, Acoustic fabrication via the assembly and fusion of particles, Adv. Mater. **30**, 1704507 (2018).

[29] M. Baudoin, J.-C. Gerbedoen, A. Riaud, O. B. Matar, N. Smagin, and J.-L. Thomas, Folding a focalized acoustical vortex on a flat holographic transducer: Miniaturized selective acoustical tweezers, Sci. Adv. **5**, eaav1967 (2019).

[30] A. Riaud, M. Baudoin, O. Matar, L. Becerra, and J.-L. Thomas, Selective Manipulation of Microscopic Particles with Precursor Swirling Rayleigh Waves, Phys. Rev. Appl. **7**, 024007 (2017).

[31] Verasonics, Vantage Volume Data Sheet, available at https://verasonics.com/matrix-array/ (2018).

[32] See the Supplemental Material at http://link.aps.org/supplemental/10.1103/PhysRevApplied.12.064055 for further details about experimental and simulated calculations and results, as well as videos of experiments.

[33] B. W. Drinkwater and P. D. Wilcox, Ultrasonic arrays for non-destructive evaluation: A review, NDT E Int. **39**, 525 (2006).

[34] J. Russel, Ph.D. thesis, Mechanical Engineering Department, Imperial College London, 6 (2010), p. 24.

[35] K. Martin and R. Fernandez, A thermal beam-shape phantom for ultrasound physiotherapy transducers, Ultrasound Med. Biol. **23**, 1267 (1997).

[36] L. Cox, A. Croxford, B. Drinkwater, and A. Marzo, Acoustic lock: Position and orientation trapping of non-spherical sub-wavelength particles in mid-air using a single-axis acoustic levitator, Appl. Phys. Lett. **113**, 054101 (2018).

[37] S. Inoue, S. Mogami, T. Ichiyama, A. Noda, Y. Makino, and H. Shinoda, Acoustical boundary hologram for macroscopic rigid-body levitation, J. Acoust. Soc. Am. **145**, 328 (2019).

[38] L. Cox, K. Melde, A. Croxford, P. Fischer, and B. W. Drinkwater, Data for: "Acoustic Hologram Enhanced Phased Arrays for Ultrasonic Particle Manipulation," Zenodo, https://doi.org/10.5281/zenodo.3463410 (2019).